VU Research Portal

Dynamics of diverse coherences in primary charge separation of bacterial reaction center at 77 K revealed by wavelet analysis

Ma, Fei; Romero, Elisabet; Jones, Michael R.; Novoderezhkin, Vladimir I.; Yu, Long Jiang; van Grondelle, Rienk

Link to publication in VU Research Portal

ORIGINAL ARTICLE

Dynamics of diverse coherences in primary charge separation of bacterial reaction center at 77 K revealed by wavelet analysis

Fei Ma[1,2] · Elisabet Romero[2,5] · Michael R. Jones[3] · Vladimir I. Novoderezhkin[4] · Long-Jiang Yu[1] · Rienk van Grondelle[2]

Abstract

To uncover the mechanism behind the high photo-electronic conversion efficiency in natural photosynthetic complexes it is essential to trace the dynamics of electronic and vibrational quantum coherences. Here we apply wavelet analysis to two-dimensional electronic spectroscopy data for three purple bacterial reaction centers with mutations that produce drastically different rates of primary charge separation. From the frequency distribution and dynamic evolution features of the quantum beating, electronic coherence with a dephasing lifetime of ~50 fs, vibronic coherence with a lifetime of ~150 fs and vibrational/vibronic coherences with a lifetime of 450 fs are distinguished. We find that they are responsible for, or couple to, different specific steps during the primary charge separation process, i.e., intradimer charge transfer inside the special bacteriochlorophyll pair followed by its relaxation and stabilization of the charge-transfer state. The results enlighten our understanding of how quantum coherences participate in, and contribute to, a biological electron transfer reaction.

Keywords Bacterial reaction center · Primary charge separation · Quantum coherence · Wavelet analysis

Introduction

Photosynthesis, consisting of a series of complex reactions, utilizes solar energy to power the living organisms. The total energy yield of photosynthesis is not high due to energy dissipation associated with many of the component steps. However, the primary processes of light harvesting, excitation transfer and photo-electronic conversion are conducted with a high quantum efficiency. Remarkably, in Reaction center (RC) pigment-protein complexes, where harvested solar energy is converted into a trans-membrane electrochemical potential, the quantum efficiency for photo-electronic conversion (charges separated per photon absorbed) is close to an unity (Parson and Warsher 2008).

Many efforts have been made to understand this near-unity quantum efficiency. X-ray crystal structures show that light-powered charge separation is accomplished by (bacterio) chlorin cofactors embedded in a protein matrix that spans the photosynthetic membrane (Feher et al. 1989). In the RC of the purple bacterium *Rhodobacter* (*Rba.*) *sphaeroides* these cofactors are a pair of bacteriochlorophyll (BChl) *a* often called special pair (P), two monomeric BChl *a* (B) and two bacteriopheophytin (BPhe) *a* (H) molecules arranged in two branches around an axis of quasi twofold symmetry. These cofactors exhibit near-discrete absorption bands with maxima around 880 nm (P pair), 800 nm (B_A/B_B) and 755 nm (H_A/H_B) at 77 K (Fig. S1). Ultrafast time-resolved spectroscopy has shown that charge separation is initiated from

✉ Fei Ma
  fma@ibcas.ac.cn

✉ Long-Jiang Yu
  longer@ibcas.ac.cn

[1] Key Laboratory of Photobiology, Institute of Botany, Chinese Academy of Sciences, Nanxincun 20, Xiangshan, Beijing 100093, China

[2] Department of Biophysics, Faculty of Sciences, VU University Amsterdam, De Boelelaan 1081, 1081 HV Amsterdam, The Netherlands

[3] School of Biochemistry, University of Bristol, Biomedical Sciences Building, University Walk, Bristol BS8 1TD, UK

[4] A. N. Belozersky Institute of Physico-Chemical Biology, Moscow State University, Leninskie Gory, Moscow, Russia 119992

[5] Present Address: Institute of Chemical Research of Catalonia, Barcelona Institute of Science and Technology, E-43007 Tarragona, Spain

the first singlet excited state of P (P*), with an electron being transferred to a ubiquinone (Q_A) via the intervening B_A and H_A that make up the "active branch" of cofactors. The $P^* \to P^+B_A^-$, $P^+B_A^- \to P^+H_A^-$ and $P^+H_A^- \to P^+Q_A^-$ Electron transfer (ET) processes occur with time constants of 1.4 ps, ~0.5 ps and ~200 ps, respectively, at 77 K (Brederode and Jones 2000;; Heathcote and Jones 2012). If P is not excited directly, energy transfer occurs according to the sequence $H \to B \to P$ within 200 fs (Jordanides et al. 2001). Coherent nuclear motion coupling (Vos et al. 1993; Novoderezhkin et al. 2004; Eisenmayer et al. 2012) and mixed electronic-vibrational (vibronic) coherence between excitonic and Charge-transfer (CT) states (Novoderezhkin et al. 2015) have been revealed to facilitate both charge separation (Romero et al. 2014; Fuller et al. 2014; Ma et al. 2018) and energy transfer (Ryu et al. 2014; Flanagan et al. 2016; Paleček et al. 2017) processes in both purple bacterial RCs and their plant counterparts. While most of the studies on bacterial RCs involved the coherent mechanism in energy transfer (Ryu et al. 2014; Flanagan et al. 2016; Niedringhaus et al. 2018), our work focused on the mechanism in the detailed primary charge separation.

Reactions occurring between cofactors in photosynthetic complexes are strongly influenced by their protein environment. This not only positions cofactor molecules with specific configurations at particular distances and orientations with respect to one another, resulting in excitons delocalized in the coherent domain, but also interacts with cofactor molecules via system-bath coupling (Tihana et al. 2017). Furthermore, some parts of the protein matrix can participate in the reaction process, for example by enhancing/reducing driving force along a reaction coordinate (Eisenmayer et al. 2013). The process focused on in this work, the primary charge separation step $P^* \to P^+B_A^-$, is a typical example. It principally consists of two sub-steps: a fast partial charge separation inside P ($P^* \to P^*P_A^{+\delta}P_B^{-\delta}$, with a time constant of 110 fs) and the relatively slower ET from P to B_A ($P^*P_A^{+\delta}P_B^{-\delta} \to P^+B_A^-$, 1.4 ps) (Fig. 1) (Ma et al. 2019). The fast initial sub-step is achieved through strong electronic coupling between the two closely apposed BChl a molecules in the P dimer that induces CT character into the lowest exciton state (Moore et al. 1999). Note that $P^*P_A^{+\delta}P_B^{-\delta}$ is sometimes simplified as $P_A^+P_B^-$, as in (Eisenmayer et al. 2012; Ma et al. 2019). The subsequent slower step involves
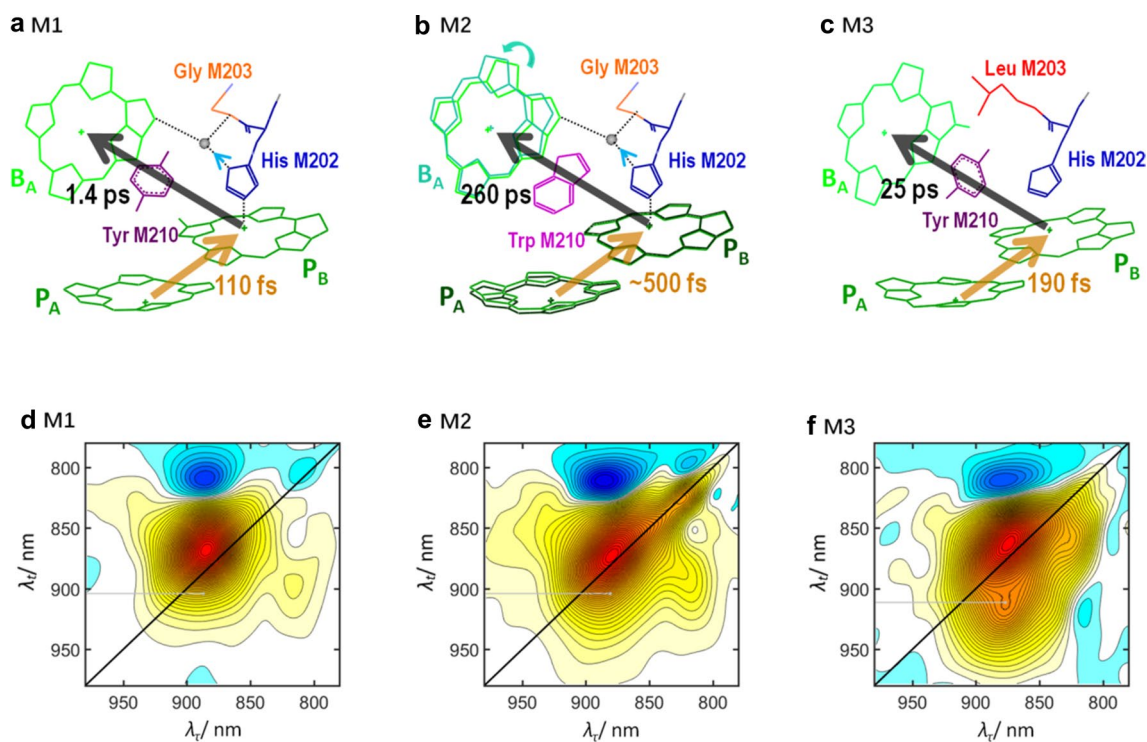
Fig. 1 Scheme for primary charge separation in mutant RCs **M1** (**a**), **M2** (**b**) and **M3** (**c**). The X-ray crystal structures of **M1** and **M3** are from PDB records 1QOV (McAuley et al. 1999) and 2BOZ (Potter et al. 2005). In **M2**, B_A and P are slightly tilted relative to one another and the weak hydrogen-bond (grey dotted line) between Tyr210 and P_B disappears as the result of the tyrosine at M210 position (purple in (**a**) and (**c**)) being replaced by a larger tryptophan (magenta in (**b**)) (McAuley et al. 2000). In **M3**, a water molecule (grey ball in (**a**) and (**b**)) linking P_B and B_A via a hydrogen-bond interaction (black dotted lines) is removed as a result of the glycine at M203 position (orange in (**a**) and (**b**)) being replaced by leucine (red in (**c**)). In all panels the dark yellow and black arrows show the two steps of primary electron transfer with time constants obtained from (Ma et al. 2019). **d–f** Absorptive 2D spectra at the population time of 100 fs. The grey points mark the location of the (P^*, $P^*P_A^{+\delta}P_B^{-\delta}$) cross peaks, their λ_t values reflect the energies of $P^*P_A^{+\delta}P_B^{-\delta}$

at least two proton displacements with surrounding amino acid and water molecules to stabilize the ET product $P^+B_A^-$ and, as a result, charge recombination is suppressed (Ivashin and Shchupak 2012; Eisenmayer et al. 2013).

Quantum phenomena are believed to contribute to the high efficiencies of the primary steps of photosynthesis (Knox 1996). Numerous efforts have been made to unravel how exactly coherent mechanisms influence ultrafast photosynthetic processes, particularly with the development of two-dimensional electronic spectroscopy (2DES) during the last two decades (Engel et al. 2007; Thyrhaug et al. 2018; Anna et al. 2014; Chenu and Scholes 2015; Romero et al. 2017a; Wang et al. 2019). Recently, different quantum beats with distinct dephasing lifetimes were distinguished (Thyrhaug et al. 2018; Ma et al. 2019; Meneghin et al. 2018), which suggests reasonable assignments of their origins as electronic, vibrational or mixed electronic-vibrational (vibronic) coherences (Irgen-Gioro et al. 2019; Gelin et al. 2019; Meneghin et al. 2018).

Our recent work with three mutant RCs of purple bacterial *Rba. sphaeroides* showed that losing or suppressing quantum coherence correlates with a slower electron transfer rate (Ma et al. 2019). All the three RCs, named **M1**, **M2** and **M3** (Fig. 1), were based on a mutation that replaces an alanine at position 260 of the M-polypeptide with tryptophan (AM260W). This causes the RC to assemble without the Q_A ubiquinone acceptor, blocking long-lived charge separation and ensuring that the RC remains in an active condition during the 2DES measurements (i.e., charge separated states do not accumulate) (Ma et al. 2018, 2019). The AM260W mutation does not influence the fast electron transfer processes associated with primary charge separation. In the **M1** mutant, which had only this AM260W change, the $P^* \rightarrow P^+B_A^- \rightarrow P^+H_A^-$ ET rates were therefore essentially identical to those in the wild-type RC. The **M2** mutant combined AM260W with an additional replacement of the tyrosine at position 210 of the M-polypeptide with tryptophan (denoted YM210W), whereas the **M3** mutant combined AM260W with replacement of glycine at position 203 of the M-polypeptide with leucine (denoted GM203L). In each case the additional mutation increased the time constant of the primary charge separation, from 1.4 ps (Fig. 1a) to 260 ps for **M2** (Fig. 1b) and 25 ps for **M3** (Fig. 1c), by either changing the relative orientations of the cofactors and removing the dipole of the OH group of tyrosine M210 in **M2** (McAuley et al. 2000) or removing the linkage between P_B and B_A mediated by a water molecule in **M3** (Potter et al. 2005). Several frequencies were revealed, principally 160 and 115 cm^{-1} modes assigned to vibrational/vibronic coherences and a short-lived electronic coherence whose frequency was difficult to determine. In this work, to investigate the dynamics of various quantum coherences we apply wavelet analysis

(Prior et al. 2013; Volpato and Collini 2015; Romero et al. 2017b) to 2DES data of the three mutant RCs. The results identify correlations between specific coherences and reaction steps, providing a way to identify real electronic coherence and estimate its dephasing lifetime.

Material and methods

Experiment

The details of the three mutant RCs preparation, 2DES setup and 77 K measurements for the experimental data presented here can be found in Ref. (Ma et al. 2019).

Wavelet analysis

Details of the wavelet analysis, i.e., Time–frequency transform (TFT), applied to the 2DES data can be found in Ref. (Romero et al. 2017b). In principle, the transformation is applied to T. Firstly, a mother wavelet function with one variable T, $\Psi(T)$, is translated into a wavelet atom function with two variables u and s, $\Psi_{us}^*(T)$:

$$\Psi_{us}^*(T) = \frac{1}{\sqrt{s}}\Psi\left(\frac{T-u}{s}\right) \tag{1}$$

Then TFT is applied to the oscillatory part of the 2D spectra with $\Psi_{us}^*(T)$ as effective basis:

$$S_{TFT}(\lambda_\tau, \lambda_t, u, s) = \int_{-\infty}^{+\infty} S(\lambda_\tau, \lambda_t, T)\Psi_{us}^*(T)dT \tag{2}$$

u and s represent frequency and TFT population time (T', whose values were identical with population time T), so transformation at one specific point (λ_τ, λ_t) results in a time–frequency plot, $S_{TFT}(u, s)$, while time-resolved 2D frequency maps are obtained if transforming over all the (λ_τ, λ_t) points. In this work, complex Morlet wavelet was chosen as mother wavelet function:

$$\Psi(T) = (\pi F_b)^{-0.5}\exp(-2i\pi F_c T)\exp(-T^2/F_b) \tag{3}$$

where F_b is a bandwidth parameter and F_c is the wavelet cener frequency. F_b strongly influences the frequency and time resolution, with opposite effects. So a range of F_b from 0.1 to 10 has been explored with F_c fixed to 1. We selected the optimal values to compromise between the time and frequency resolution, $F_c = 1$ and $F_b = 3$. The transformation was employed to the real rephasing 2D spectra over the population time range of 0–1000 fs with 8 fs step. The time and frequency resolution after TFT were 14 fs and 29 cm^{-1}.

Results

The TFT method can not only extract the main frequency components from the beating signals as a Fourier transform, but also reveal their temporal evolutions. TFT of an oscillatory trace at $(\lambda_\tau, \lambda_t)$ point in the 2D spectra results in a bi-dimensional time–frequency plot. The plots for the $(P^*, P^*P_A^{+\delta}P_B^{-\delta})$ position are shown in Fig. 2. The positions (pointed out in Fig. 1d–f) were at (884.3, 902.0) nm for **M1** and (878.0, 906.0) nm for **M3**. In **M2**, a similar position at (882.5, 902.0) nm was chosen to compare with the other two, although no band corresponding to $P^*P_A^{+\delta}P_B^{-\delta}$ was resolved.

For **M1** there were two main frequency components centered at 160 and 220 cm^{-1}, and one weaker component centered at 100 cm^{-1}. The 100 and 160 cm^{-1} components remained until 600 fs while the 220 cm^{-1} component nearly disappeared by 200 fs. Furthermore, there seemed to be a correlation between the decay of the 220 cm^{-1} band and the rise of the 160 cm^{-1} bands.

The plot for **M2** exhibited three differences from that of **M1**. First, the 100 cm^{-1} band was nearly invisible. Second, the 160 cm^{-1} band persisted over a longer time period up to 800 fs and took longer to reach its maximal amplitude (~400 fs, compared to ~170 fs for **M1**). Lastly and most importantly, the short-lived band located at 260 cm^{-1} became much weaker.

For **M3** the 100 cm^{-1} band was only slightly visible and the 160 cm^{-1} band evolved in a similar fashion as for **M2**. The short-lived band at higher frequency was much broader than for the other two RC mutants, spreading from 250 to 450 cm^{-1} with a maximum at ~330 cm^{-1}.

These results unveiled two long-lived (600–800 fs) and one short-lived (< 200 fs) oscillatory contributions coexisting in the $(P^*, P^*P_A^{-\delta}P_B^{+\delta})$ cross peak. Comparing the three RC mutants, the frequency values for the long-lived components were similar while the values for

the short-lived component varied. The frequency of the latter (220 and 330 cm^{-1} for **M1** and **M3**, respectively) was approximately equal to the energy gap between P* and $P^*P_A^{-\delta}P_B^{+\delta}$ in the corresponding RC mutant (220 and 350 cm^{-1}, respectively), estimated by setting the P energy using the peak value in the absorption spectrum (884.3 and 878.0 nm, see Fig. S1) and the $P^*P_A^{-\delta}P_B^{+\delta}$ energy with the λ_t value of the $(P^*, P^*P_A^{-\delta}P_B^{+\delta})$ cross peak in the 2DES spectrum (902.0 and 906.0 nm, respectively, see Fig. 1d–f). Although there were ~200 and ~330 cm^{-1} bands appearing in the resonance Raman spectrum of P, the 220 cm^{-1} beating in **M1** and the 330 cm^{-1} beating in **M3** cannot be with vibrational origin. It is because that (1) the lifetime of vibrational coherence should be much longer than 200 fs and (2) vibrational coherence should not be sample-dependent, if the 220 and 330 cm^{-1} beatings arose from vibration coherence, they both should appear in all the three mutants. Coherent states oscillates with a frequency equal to their energy difference (Engel et al. 2007), and thus the results indicated that the coherence between P* and $P^*P_A^{-\delta}P_B^{+\delta}$ has electronic character. The much broader 350 cm^{-1} band for **M3** reflected a disorder-induced spread of the electronic gap between the P* and $P^*P_A^{-\delta}P_B^{+\delta}$ levels, which may be enhanced when the coupling between P* and $P^*P_A^{-\delta}P_B^{+\delta}$ decreases as a result of removing the water molecule. The much weaker 260 cm^{-1} oscillation amplitude for **M2** is consistent with the observation that nearly no $P^*P_A^{-\delta}P_B^{+\delta}$ state is formed in the **M2** RC (Ma et al. 2019).

While a TFT analysis of a specific oscillatory trace is already able to distinguish various coherences, a TFT analysis over the whole of a 2D spectrum provides thorough dynamic information on the coherences during the charge separation process. TFT analysis over the whole spectrum results in time-resolved 2D frequency maps (Romero et al. 2017b), which are the amplitude distributions of each frequency in the 2D spectra, and their corresponding evolution dynamics, i.e., the wavelet traces. Accordingly we investigated the coherences with conserved frequencies at

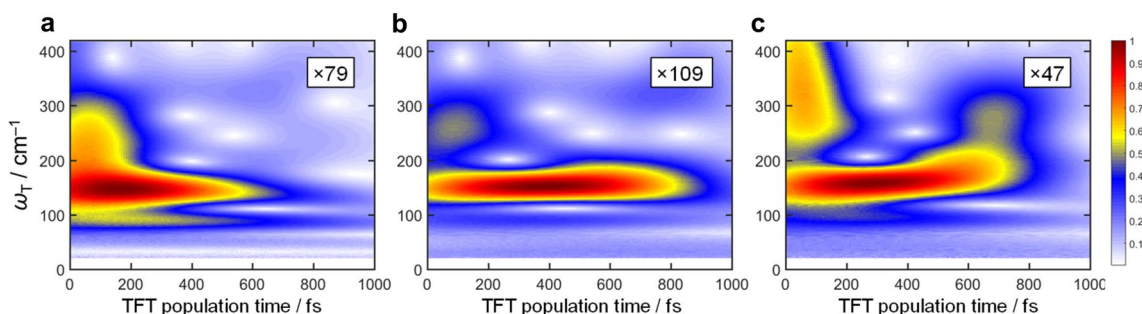**Fig. 2** Time–frequency plots of the real rephasing oscillatory traces at respective $(P^*P_A^{+\delta}P_B^{-\delta})$ positions for mutant RCs **M1** (**a**), **M2** (**b**) and **M3** (**c**). Each plot is normalized to its maximal amplitude. The value in the right-top corner of each panel is the ratio between the maximal amplitude of the 2D spectrum at population time $T=0$ fs and the maximal amplitude of the plot

110 cm^{-1} and 160 cm^{-1}, and sample-dependent frequencies at 220, 260, 330 cm^{-1}. Because the majority of excitation is on P, all of the 2D frequency maps predominantly reflect information on P.

Time-resolved 2D frequency maps of **M1** at 220, 160 and 110 cm^{-1} and 30, 250 and 600 fs (i.e., $S_{\text{TFT}}\left(\lambda_\tau, \lambda_t, u, s\right)$ at selected frequency u and selected population time s) are shown in Fig. 3a, c, e. For each frequency, wavelet traces at selected $\left(\lambda_\tau, \lambda_t\right)$ positions (pointed by colored circles) are shown in Fig. 3b, d, f. For both the 160 cm^{-1} and 110 cm^{-1} mode the shape of the 2D frequency map remained nearly unchanged with time (Fig. 3c, e), with similar evolution dynamics at different positions in the map. The maps were dominated by a diagonal peak at the P position, such a diagonal-only shape usually representing a vibrational coherence (Romero et al. 2014). The wavelet traces reached the maximal amplitude at round

210 fs (Fig. 3d, f), then decayed with a time constant of 450 fs. The behavior for the 220 cm^{-1} mode was more complicated, with the shape of the 2D frequency map changing with time (Fig. 3a). At 30 fs it consisted of a diagonal peak at the P position and two cross peaks that were nearly symmetrical along the diagonal, at around the $(P^*, P^*P_A^{-\delta}P_B^{-\delta})$ and $(P^*P_A^{-\delta}P_B^{-\delta}, P^*)$ positions. These cross peaks disappeared after 400 fs. Cross peaks at $T = 0$ indicate electronic coupling, and thus the symmetrical cross peaks corresponding to the P* and $P^*P_A^{-\delta}P_B^{-\delta}$ positions demonstrate electronic coherence between the two. As the wavelet dynamics show (Fig. 3b), they reached the maximal amplitude at around 100 fs (with an approximate time constant of ~45 fs) and then decayed with a time constant of 150 fs. It was noticeable that this 150 fs decay correlated with the rise of the 160 cm^{-1} and 110 cm^{-1} wavelet traces (Compare Fig. 3b with 3(d,f)). Subsequent to
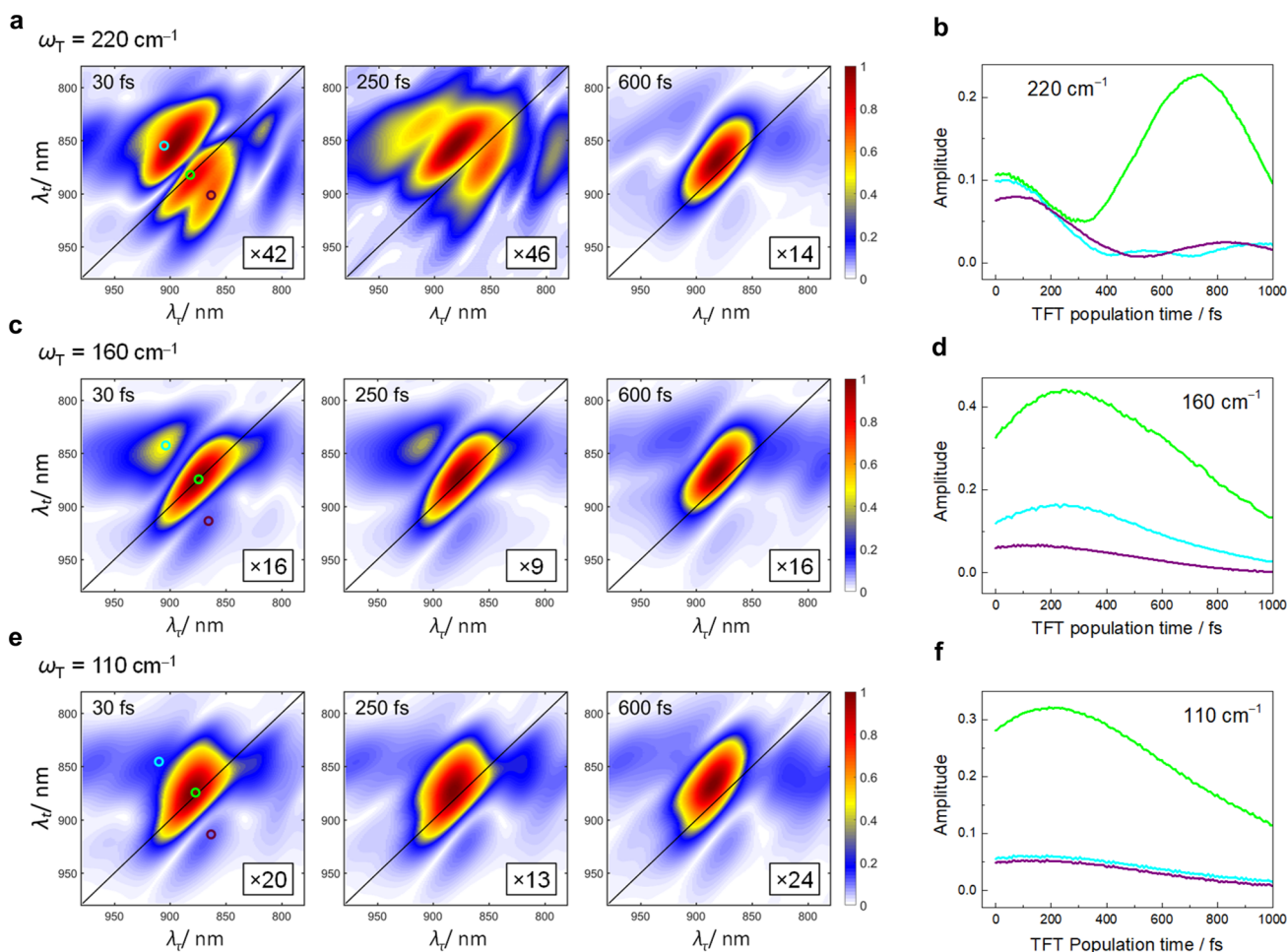
Fig. 3 Dynamics of various coherences in mutant **M1**: 220 cm^{-1} (**a, b**), 160 cm^{-1} (**c, d**) and 110 cm^{-1} (**e, f**). 2D frequency maps at selected TFT population times T' are shown in (**a, c, e**) and wavelet traces at selected positions in (**b, d, f**). In (**a, c, e**), each frequency map is normalized to its maximal amplitude. The value in the right-bottom corner of each panel is the ratio between the maximal amplitude of the 2D spectrum and the maximal amplitude of the frequency map at the same population time T. The colored circles in each 30 fs panel indicate the positions of the selected 2D wavelet traces in (**b, d, f**)

this 150 fs decay, another diagonal peak rose and became dominant after 500 fs (Fig. 3b). It was also apparent in the wavelet dynamics that while the two cross peak wavelet traces decayed to zero, another rise and decay appeared in the 300–1000 fs range of the diagonal peak wavelet trace (Fig. 3b). This additional dynamics with an extraordinarily high amplitude may have arisen from an interference artifact (Romero et al. 2017b) between the 220 and 160 cm^{-1} frequencies, because (1) the period of the dynamic feature, ~620 fs corresponding to 57 cm^{-1}, was inversely proportional to the frequency spacing between the 220 and the 160 cm^{-1} frequencies (60 cm^{-1}) and (2) the shape of the 220 cm^{-1} frequency map at long time (> 400 fs) resembled that of the 160 cm^{-1} one. To summarize, the time constants for the 220 cm^{-1} beating connecting P* and

P*$P_A^{-\delta}P_B^{-\delta}$ are ~45 fs and a 150 fs, and for both the 160 cm^{-1} and 110 cm^{-1} beatings are 150 fs and 450 fs (Table 1).

For **M2**, since the 110 cm^{-1} oscillation frequency does not appear in the (P*, P*$P_A^{-\delta}P_B^{-\delta}$) time–frequency plot nor in the summary Fourier-transform spectrum (see (Ma et al. 2019)), 2D frequency maps and wavelet traces are shown in Fig. 4 only for the 260 and 160 cm^{-1} modes. As for **M1**, the 160 cm^{-1} frequency map was dominated by a diagonal peak at the P position (Fig. 4c), but the main wavelet trace took a longer time, 400 fs, to reach the maximal amplitude (with an approximate time constant of ~200 fs) than the 210 fs for **M1** (Fig. 4d). It then decayed with a time constant of 450 fs. The shape and the timescale indicate that the 160 cm^{-1} beating also corresponds to a vibrational coherence. For the 260 cm^{-1} mode, although the frequency

Table 1 Time constants for the various beating components in the three mutant RCs

	Sample-dependent component			160 cm^{-1}		110 cm^{-1}	
	Frequency (cm^{-1})	Rise (fs)	Decay (fs)	Rise (fs)	Decay (fs)	Rise (fs)	Decay (fs)
M1	220	~45	150	150	450	150	450
M2	260	~40	140	200	450	[a]	[a]
M3	330	~60	140	140	450	140	450

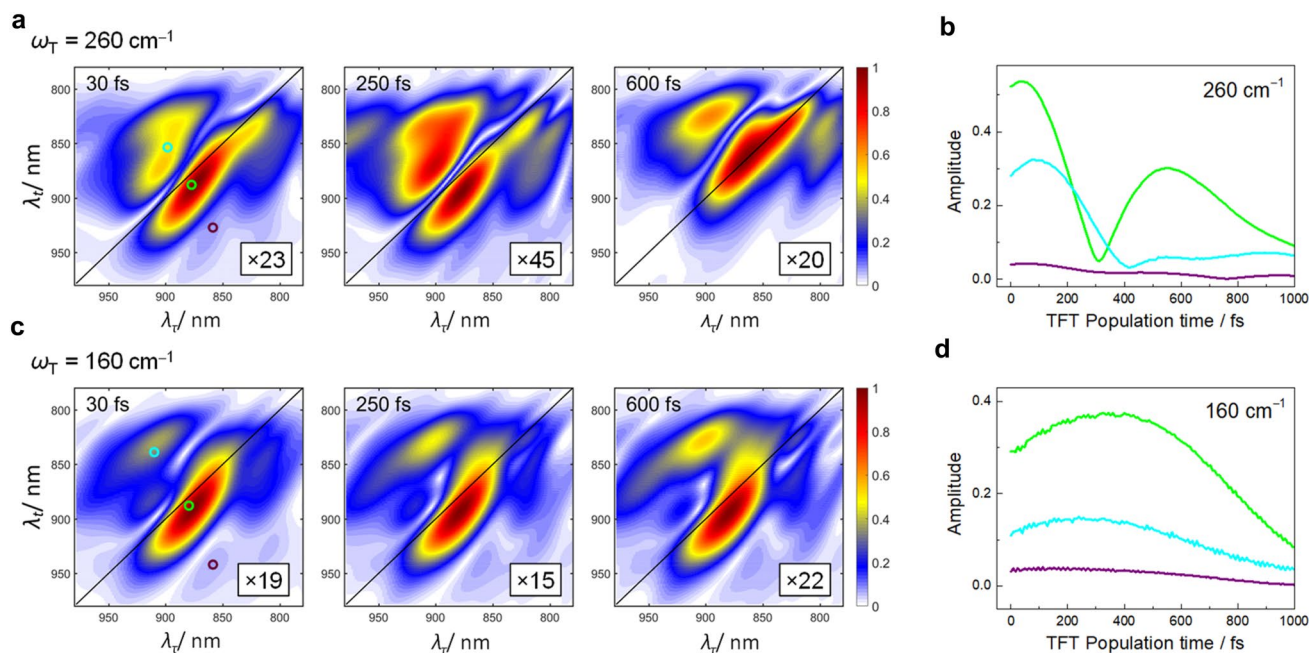[a]The 110 cm^{-1} component did not appear in **M2**

Fig. 4 Dynamics of various coherences in mutant **M2**: 260 cm^{-1} (**a, b**) and 160 cm^{-1} (**c, d**). 2D frequency maps at selected TFT population times T' are shown in (**a, c**) and wavelet traces at selected positions in (**b, d**). In (**a, c**), each frequency map is normalized to its maximal amplitude. The value in the right-bottom corner of each panel is the ratio between the maximal amplitude of the 2D spectrum and the maximal amplitude of the frequency map at the same population time T. The colored circles in each 30 fs panel indicate the positions of the selected 2D wavelet traces in (**b, d**)

map did not exhibit a definite feature for electronic coherence as for **M1** and **M3** (Fig. 4a), the wavelet trace showed fast rise and decay with time constants of ~40 fs and 140 fs (Fig. 4b), and thus it may reflect an electronic coherence. However, considering the particularly weak amplitude in the time–frequency plot (Fig. 2b), the 260 cm^{-1} coherence is actually not employed in the charge separation process. There is also an interference artifact after 300 fs, with relatively weaker amplitude than in **M1**.

The situation for **M3** (Fig. 5) was similar to that of **M1**. The predominantly diagonal shape of the 2D frequency maps and the timescales of the 160 and 110 cm^{-1} frequencies indicated that they correspond to vibrational coherence with characteristic time constants of 140 fs and 450 fs. The 2D frequency map of the 330 cm^{-1} mode at 30 fs consisted of a P diagonal peak and two cross peaks at (P*, $P^*P_A^{-\delta}P_B^{-\delta}$) and ($P^*P_A^{-\delta}P_B^{-\delta}$, P*) positions. Its main

feature reached the maximal amplitude at around 180 fs and then decayed with a time constant of 140 fs. As with **M1**, the short-lived 330 cm^{-1} beating connecting P* and $P^*P_A^{-\delta}P_B^{-\delta}$ has characteristic time constants of ~60 fs and 140 fs. The interference artifact in the 350–1000 fs range was much weaker than in **M1** and **M2**, consistent with the fact that the frequency spacing between the 330 and 160 cm^{-1} modes is much further from being resonant with the feature's oscillation period (~560 fs, corresponding to 63 cm^{-1}).

Discussion

The TFT results described above successfully distinguished the short-lived electronic coherence in mutants **M1** and **M3**, which would not be a straightforward task
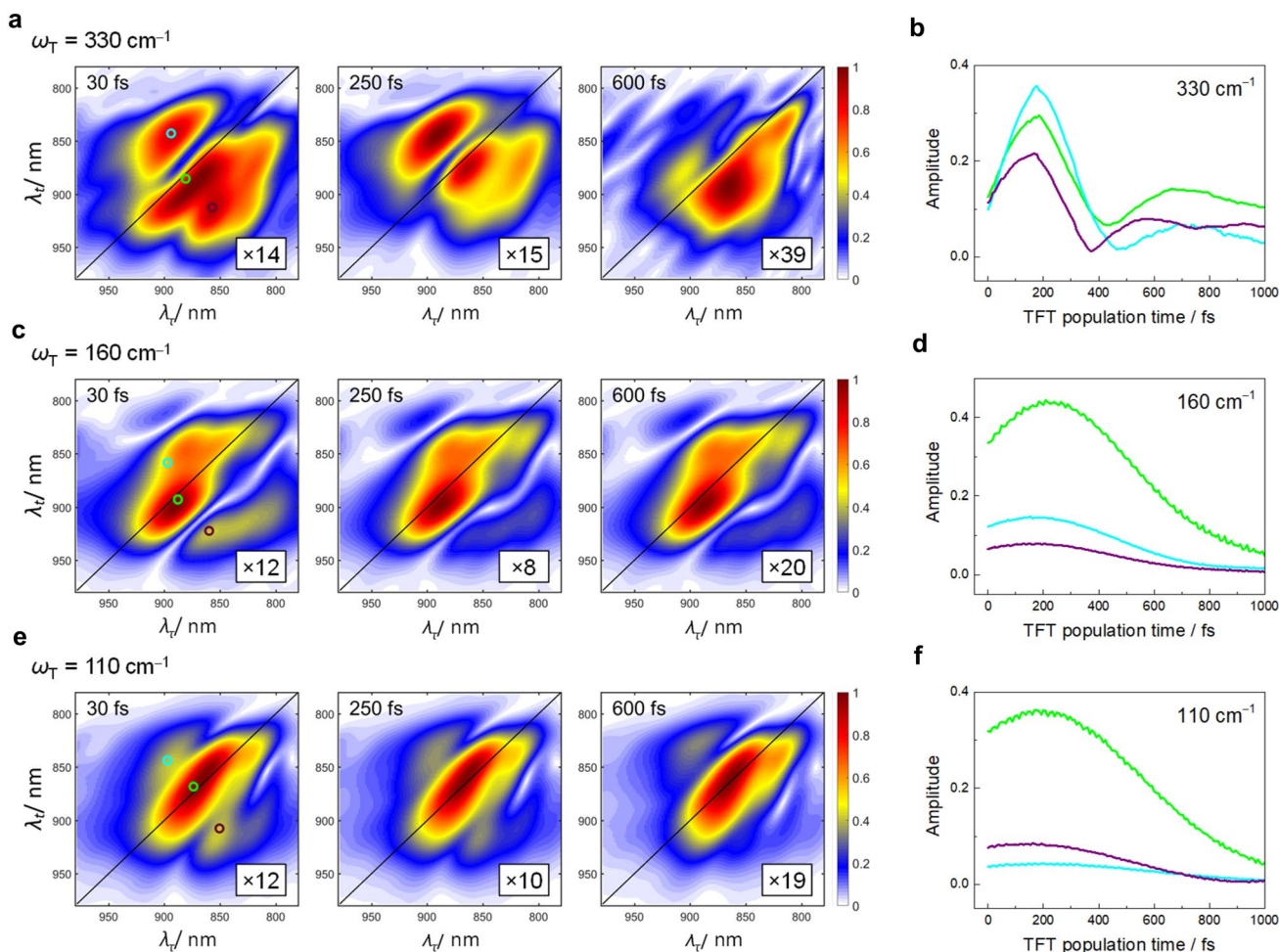

Fig. 5 Dynamics of various coherences in mutant **M3**: 330 cm^{-1} (**a**, **b**), 160 cm^{-1} (**c**, **d**) and 110 cm^{-1} (**e**, **f**). 2D frequency maps at selected TFT population times T' are shown in (**a**, **c**, **e**) and wavelet traces at selected positions in (**b**, **d**, **f**). In (**a**, **c**, **e**), each frequency map is normalized to its maximal amplitude. The value in the right-bottom corner of each panel is the ratio between the maximal amplitude of the 2D spectrum and the maximal amplitude of the frequency map at the same population time T. The colored circles in each 30 fs panel indicate the positions of the selected 2D wavelet traces in (**b**, **d**, **f**)

without this analysis. Furthermore the rise and decay dynamics of various beating components were obtained, helping understand which step of the charge separation process they couple to and the functional roles they play.

In previous work (Ma et al. 2019) we derived the following dynamic schemes for the three RCs:

$$P^* \xrightarrow{110fs} P^*P_A^{+\delta}P_B^{-\delta} \xrightarrow{1.4ps} P^+B_A^- \xrightarrow{430fs} P^+H_A^-$$

for **M1**, $P^* \xrightarrow{260fs} P^+B_A^- \xrightarrow{510fs} P^+H_A^-$ for **M2** and

$P^* \xrightarrow{190fs} P^*P_A^{+\delta}P_B^{-\delta} \xrightarrow{25ps} P^+B_A^- \xrightarrow{450fs} P^+H_A^-$ for **M3**. In both **M1** and **M3**, the $P^*P_A^{-\delta}P_B^{-\delta}$ state forms promptly, with a time constant of 110 fs for **M1** and 190 fs for **M3**, and acts as a charge separation intermediate. In this work, through TFT analysis, more complex evolution dynamics appear for the short-lived oscillation frequency that connects P^* and $P^*P_A^{-\delta}P_B^{-\delta}$. The corresponding wavelet trace consists of a rise and a decay component, with the time constants of 45 fs and 150 fs for **M1** and 60 fs and 140 fs for **M3**.

Purely electronic charge migration driven by the electronic coherence of a superposition state is extraordinarily fast, e.g., on sub-femtosecond time scale for an individual molecule in vacuum (Wörner et al. 2017). Nuclear wavepacket motions triggered by the superposition of electronic states leads to an ultrafast dephasing of the electronic coherence on the time scale from a few to a few tens of femtoseconds (Duan et al. 2017). The time constants of the rise component, 45 fs for **M1** and 60 fs for **M3**, are close to the upper estimate of electronic dephasing timescale, ~55 fs, derived from the anti-diagonal width (Duan et al. 2017) of the P ground-state bleach band. Furthermore, they are similar to the electronic dephasing lifetimes determined in other photosynthetic proteins such as PSII RC (Romero et al. 2017b; Novoderezhkin et al. 2017), Fenna–Matthews–Olson complex and light-harvesting complex (Thyrhaug et al. 2018; Irgen-Gioro et al. 2019; Duan et al. 2017). Thus we attribute this ~50 fs component to the dephasing lifetime of the electronic coherence between P^* and $P^*P_A^{-\delta}P_B^{-\delta}$. Comparing **M1** and **M3**, the rise component is more distinct in **M3** while it is more like an unchanged amplitude in **M1**. Furthermore, the maximum amplitude is reached earlier in **M1** than in **M3**. The energy gap between P^* and $P^*P_A^{-\delta}P_B^{-\delta}$ in **M3**, 330 cm^{-1}, is larger than in **M1**, 220 cm^{-1}. All these differences reflect different electronic structures of the P dimer due to the CT-exciton mixing. This effect may also be responsible for the negligible $P^*P_A^{-\delta}P_B^{-\delta}$ state formation in **M2**. These results show that electronic coherence is essential for the $P^*P_A^{-\delta}P_B^{-\delta}$ state formation and as a result the rate of the primary charge separation.

The ~150 fs decay time constants are consistent with the first population time, 110 fs for **M1** and 190 fs for **M3** which was assigned to the formation time constants of the intra-dimer CT state and the electronic dephasing lifetimes (Ma et al. 2019). Now with the help of TFT analysis, we found that 100–200 fs lifetime is overvalued for a purely electronic coherence, which should eliminate the interference of nuclear motions. The ~150 fs component is therefore attributed to a relaxation and stabilization of $P^*P_A^{-\delta}P_B^{-\delta}$, which is achieved by coupling specific vibrational modes (Eisenmayer et al. 2012), i.e., vibronic coherence. As a result, both the ~50 fs electronic and ~150 fs vibronic coherences are involved in the $P^*P_A^{-\delta}P_B^{-\delta}$ formation process.

The sample-independent frequency and characteristic timescale of the 160 cm^{-1} beating indicate a vibrational coherence. In **M1** and **M3**, the rise and decay time constants are ~150 fs and ~450 fs, close to the population dynamic time constants, 110 fs/190 fs and 430 fs/450 fs for **M1**/**M3** (Ma et al. 2019). The ~150 fs rise corresponds to the formation and relaxation of $P^*P_A^{-\delta}P_B^{-\delta}$. The assignment of the ~450 fs decay is less straightforward, because it is close to the time constant of the third step, $P^+B_A^- \rightarrow P^+H_A^-$, but appears just following the first ~150 fs component in the dynamic curves. It is the typical kinetic character that a subsequent step appears before its preceding one when it is faster. As a result, although the electron transfer sequence is $P^* \xrightarrow{110fs} P^*P_A^{+\delta}P_B^{-\delta} \xrightarrow{1.4ps} P^+B_A^- \xrightarrow{430fs} P^+H_A^-$ in **M1** and $P^* \xrightarrow{190fs} P^*P_A^{+\delta}P_B^{-\delta} \xrightarrow{25ps} P^+B_A^- \xrightarrow{450fs} P^+H_A^-$ in **M3**, virtually the 110 fs/190 fs, 430 fs/450 fs and 1.4 ps/25 ps components appear sequentially in the dynamics. Therefore, the 160 cm^{-1} vibrational coherence may start activation right after $P^*P_A^{-\delta}P_B^{-\delta}$ is formed and then deactivate synchronously with the electron transfer process from P to B$_A$. In **M2**, the decay time constant, 450 fs, is the same as in **M1** and **M3** while the rise is a little slower. This difference may reflect a different activation process of this mode, bypassing the $P^*P_A^{-\delta}P_B^{-\delta}$ state. However, the 160 cm^{-1} vibrational coherence itself seems to not play an essential role for charge separation, because its lifetime in the three mutant RCs is nearly invariant.

The situation for the 110 cm^{-1} beating in **M1** and **M3** is similar to that for the 160 cm^{-1} beating. The absence of the 110 cm^{-1} component in **M2** is correlated with the absence of the $P^*P_A^{-\delta}P_B^{-\delta}$ state and the much slower charge separation, suggesting a necessary role for the charge separation inside P and possibly from P to B. Theoretical studies support this argument, postulating that the ~110 cm^{-1} vibrational mode is coupled with the electron transfer dynamics within the P dimer (Novoderezhkin et al. 2004), or from P to $P^+B_A^-$ (Eisenmayer et al. 2012), by effectively removing the barrier for charge separation and initiating a directional displacement of electron density. The ~150 fs rise and ~450 fs decay components in the wavelet dynamics may reflect its coupling with $P^*P_A^{-\delta}P_B^{-\delta}$ formation and electron transfer from P

to B_A. If this is the case, the 110 cm^{-1} beating should have a vibronic (vibrations in the excited electronic state) character. Vibronic coherences eventually turn into pure vibrational coherence in the ground electronic state due to disorder-induced melting (Gelin et al. 2019; Paleček et al. 2017). This may explain the observation that the vibrational 160 cm^{-1} and the vibronic 110 cm^{-1} beatings have similar dynamics.

Conclusion

In this work, we applied wavelet analysis to 2DES data for three mutant RCs with drastically different charge separation rates, and distinguished electronic and vibrational/vibronic coherences through investigation of the spectral and temporal features of the time-resolved 2D frequency map. Furthermore, analysis of the evolution of specific modes revealed how they participate in sub-steps of the electron transfer process. Analysis of this kind will be particularly helpful for photosynthetic proteins containing a large number of nuclear degrees of freedom, where photo-induced coherences are thought to play important roles in light-harvesting and photo-electronic conversion.

Declarations

Conflict of interest The authors wish to declare no known competing financial interests or personal relationships that have influenced the present work.

Data availability The data that support the findings of this study are available from the corresponding author upon reasonable request.

References

Anna JM, Scholes GD, van Grondelle R (2014) A little coherence in photosynthetic light harvesting. Bioscience 64:14–25

Brederode MEV, Jones MR (2000) Reaction centers of purple bacteria. Subcellular Biochemistry, 35: Enzyme-Catalyzed Electron and Radical Transfer, Kluwer Academic I Plenum Publishers, New York, pp. 621–676

Chenu A, Scholes GD (2015) Coherence in energy transfer and photosynthesis. Annu Rev Phys Chem 66:69–96

Duan H, Prokhorenko VI, Cogdell RJ, Ashraf K, Stevens AL, Thorwart M, Miller RJD (2017) Nature does not rely on long-lived electronic quantum coherence for photosynthetic energy transfer. Proc Natl Acad Sci USA 114:8493–8498

Eisenmayer TJ, de Groot HJ, van de Wetering E, Neugebauer J, Buda F (2012) Mechanism and reaction coordinate of directional charge separation in bacterial reaction centers. J Phys Chem Lett 3(6):694–697. https://doi.org/10.1021/jz201695p

Eisenmayer TJ, Lasave JA, Monti A, Groot HJMd, Buda F (2013) Proton displacements coupled to primary electron transfer in the *Rhodobacter sphaeroides* reaction center. J Phys Chem B 117:11162–11168

Engel GS, Calhoun TR, Read EL, Ahn T, Mančal T, Cheng Y, Blankenship RE, Fleming GR (2007) Evidence for wavelike energy transfer through quantum coherence in photosynthetic systems. Nature 446:782–786

Feher G, Allen JP, Okamura MY, Rees DC (1989) Structure and function of bacterial photosynthetic reaction centers. Nature 339:111–116

Flanagan ML, Long PD, Dahlberg PD, Rolczynski BS, Massey SC, Engel GS (2016) Mutations to R. Sphaeroides reaction center perturb energy levels and vibronic coupling but not observed energy transfer rates. J Phys Chem A 120(9):1479–1487

Fuller FD, Pan J, Gelzinis A, Butkus V, Senlik SS, Wilcox DE, Yocum CF, Valkunas L, Abramavicius D, Ogilvie JP (2014) Vibronic coherence in oxygenic photosynthesis. Nat Chem 6:706–711

Gelin MF, Borrelli R, Domcke W (2019) Origin of unexpectedly simple oscillatory responses in the excited-state dynamics of disordered molecular aggregates. J Phys Chem Lett 10:2806–2810

Heathcote P, Jones MR (2012) The structure-function relationships of photosynthetic reaction centers. Comprehensive Biophysics, Academic Press, Oxford, UK:115–144

Irgen-Gioro S, Gururangan K, Saer RG, Blankenship RE, Harel E (2019) Electronic coherence lifetimes of the Fenna-Matthews-Olson complex and light harvesting complex II. Chem Sci 10:10503

Ivashin NV, Shchupak EE (2012) Mechanism by which a single water molecule affects primary charge separation kinetics in a bacterial photosynthetic reaction center of *Rhodobacter sphaeroides*. Opt Spectrosc 113:474–486

Jordanides XJ, Scholes GD, Fleming GR (2001) The mechanism of energy transfer in the bacterial photosynthetic reaction center. J Phys Chem B 105:1652–1669

Knox RS (1996) Electronic excitation transfer in the photosynthetic unit: reflections on work of William Arnold. Photosynth Res 48:35–39

Ma F, Romero E, Jones MR, Novoderezhkin VI, van Grondelle R (2018) Vibronic coherence in the charge separation process of the *Rhodobacter sphaeroides* reaction center. J Phys Chem Lett 9:1827–1832

Ma F, Romero E, Jones MR, Novoderezhkin VI, van Grondelle R (2019) Both electronic and vibrational coherences are involved in primary electron transfer in bacterial reaction center. Nat Commun 10:933

McAuley KE, Fyfe PK, Ridge JP, Isaacs NW, Cogdell RJ, Jones MR (1999) Structural details of an interaction between cardiolipin and an integral membrane protein. Proc Natl Acad Sci USA 96:14706–14711

McAuley KE, Fyfe PK, Cogdell RJ, Isaacs NW, Jones MR (2000) X-ray crystal structure of the YM210W mutant reaction centre from *Rhodobacter sphaeroides*. FEBS Lett 467:285–290

Meneghin E, Volpato A, Cupellini L, Bolzonello L, Jurinovich S, Mascoli V, Carbonera D, Mennucci B, Collini E (2018) Coherence in carotenoid-to-chlorophyll energy transfer. Nat Commun 9:3160

Moore LJ, Zhou H, Boxer SG (1999) Excited-state electronic asymmetry of the special pair in photosynthetic reaction center

mutants: absorption and Stark spectroscopy. Biochemistry-US 38:11949–11960

Niedringhaus A, Policht VR, Sechrist R, Konar A, Laible PD, Bocian DF, Holten D, Kirmaier C, Ogilvie JP (2018) Primary processes in the bacterial reaction center probed by two-dimensional electronic spectroscopy. Proc Natl Acad Sci USA 115:3563–3568

Novoderezhkin VI, Yakovlev AG, van Grondelle R, Shuvalov VA (2004) Coherent nuclear and electronic dynamics in primary charge separation in photosynthetic reaction centers: a Redfield theory approach. J Phys Chem B 108:7445–7457

Novoderezhkin VI, Romero E, van Grondelle R (2015) How exciton-vibrational coherences control charge separation in the photosystem II reaction center. Phys Chem Chem Phys 17:30828–30847

Novoderezhkin VI, Romero E, Prior J, van Grondelle R (2017) Exciton-vibrational resonance and dynamics of charge separation in the photosystem II reaction center. Phys Chem Chem Phys 19:5195–5208

Paleček D, Edlund P, Westenhoff S, Zigmantas D (2017) Quantum coherence as a witness of vibronically hot energy transfer in bacterial reaction center. Sci Adv 3:e1603141

Parson WW, Warsher A (2008) Mechanism of charge separation in purple bacterial reaction centers. Advances in Photosynthesis and Respiration, 28: The Purple Phototrophic Bacteria, Springer publisher, The Netherlands, pp. 355–377

Potter JA, Fyfe PK, Frolov D, Wakeham MC, Rv G, Robert B, Jones MR (2005) Strong effects of an individual water molecule on the rate of light-driven charge aeparation in the *Rhodobacter sphaeroides* reaction center. J Biol Chem 280:27155–27164

Prior J, Castro E, Chin AW, Almeida J, Huelga SF, Plenio MB (2013) Time-frequency resolved ultrafast spectroscopy techniques using wavelet analysis. J Chem Phys 139:224103

Romero E, Ramunas A, Novoderezhkin VI, Ferretti M, Thieme J, Zigmantas D, van Grondelle R (2014) Quantum coherence in photosynthesis for efficient solar-energy conversion. Nat Phys 10:676–682

Romero E, Novoderezhkin VI, van Grondelle R (2017a) Quantum design of photosynthesis for bio-inspired solar-energy conversion. Nature 543:355–365

Romero E, Prior J, Chin AW, Morgan SE, Novoderezhkin VI, Plenio MB, van Grondelle R (2017b) Quantum-coherent dynamics in photosynthetic charge separation revealed by wavelet analysis. Sci Rep 7:2890

Ryu IS, Dong H, Fleming GR (2014) Role of electronic-vibrational mixing in enhancing vibrational coherences in the ground electronic states of photosynthetic bacterial reaction center. J Phys Chem B 118:1381–1388

Thyrhaug E, Tempelaar R, Alcocer MJP, Žídek K, Bína D, Knoester J, Jansen TLC, Zigmantas D (2018) Identification and characterization of diverse coherences in the Fenna-Matthews-Olson complex. Nat Chem 10:780–786

Tihana M, Ostroumov EE, Anna JM, van Grondelle R, Govindjee SGD (2017) Light absorption and energy transfer in the antenna complexes of photosynthetic organisms. Chem Rev 117:249–293

Volpato A, Collini E (2015) Time-frequency methods for coherent spectroscopy. Opt Express 23:20040–20050

Vos MH, Rappaport F, Lambry JC, Breton J, Martin JL (1993) Visualization of coherent nuclear motion in a membrane protein by femtosecond spectroscopy. Nature 363:320–325

Wang L, Allodi MA, Engel GS (2019) Quantum coherences reveal excitedstate dynamics in biophysical systems. Nat Rev Chem 3:477–490

Wörner HJ, Arrell CA, Banerji N, Cannizzo A, Chergui M, Das AK, Hamm P, Keller U, Kraus PM, Liberatore E, Lopez-Tarifa P, Lucchini M, Meuwly M, Milne C, Moser J, Rothlisberger U, Smolentsev G, Teuscher J, Bokhoven JAV (2017) Charge migration and charge transfer in molecular systems. Struct Dynam 4:061508